1 **The role of deep Earth dynamics in driving the flooding and emergence of New**

2 **Guinea since the Jurassic**

3

4 Lauren Harrington[1*], Sabin Zahirovic[1], Nicolas Flament[2], R. Dietmar Müller[1]

5

6 [1] EarthByte Group, School of Geosciences, University of Sydney, NSW 2006,

7 Australia

8 [2] School of Earth and Environmental Sciences, University of Wollongong,

9 Northfields Avenue, Wollongong, NSW 2522, Australia

10

11 *Corresponding author:

12 Email: lhar7322@uni.sydney.edu.au (Lauren Harrington)

13 Postal Address: Room 405, Madsen Building (F09), School of Geosciences, The

14 University of Sydney NSW 2006, Australia

15

16

17

18

19

20

21

22

23

24

25

26 **Abstract**

27 The paleogeography of New Guinea indicates fluctuating periods of flooding and

28 emergence since the Jurassic, which are inconsistent with estimates of global sea level

29 change since the Eocene. The role of deep Earth dynamics in explaining these

30 discrepancies has not been explored, despite the strongly time-dependent geodynamic

31 setting within which New Guinea has evolved. We aim to investigate the role of

32 subduction-driven mantle flow in controlling long-wavelength dynamic topography

33 and its manifestation in the regional sedimentary record, within a tectonically

34 complex region leading to orogeny. We couple regionally refined global plate

35 reconstructions with forward geodynamic models to compare trends of dynamic

36 topography with estimates of eustasy and regional paleogeography. Qualitative

37 corroboration of modelled mantle structure with equivalent tomographic profiles

38 allows us to ground-truth the models. We show that predicted dynamic topography

39 correlates with the paleogeographic record of New Guinea from the Jurassic to the

40 present. We find that subduction at the East Gondwana margin locally enhanced the

41 high eustatic sea levels from the Early Cretaceous (~145 Ma) to generate long-term

42 regional flooding. During the Miocene, however, dynamic subsidence associated with

43 subduction of the Maramuni Arc played a fundamental role in causing long-term

44 inundation of New Guinea during a period of global sea level fall.

45

46 **Key words:** New Guinea, inundation history, mantle flow, dynamic topography,

47 paleogeography

48

49

50

1. Introduction

The New Guinea margin is arguably one of the most tectonically complex settings in the world, comprising a diverse assemblage of accreted arc terranes, continental fragments, and obducted ophiolite belts (Baldwin et al., 2012). The geodynamic evolution of New Guinea in the post-Pangea period has been dominated by the long-term convergence between the Australian Plate in the southwest and the Pacific Plate in the northeast (Baldwin et al., 2012; Dow, 1977; Hill and Hall, 2003). The rapid north-northeast motion of the Australian Plate relative to the Pacific Plate since the Eocene, and the interaction with the Sunda continental promontory has resulted in oblique, arc-continent collisions and the slow growth of the island through successive accretionary episodes (Baldwin et al., 2012; van Ufford and Cloos, 2005). Such episodes include the accretion of ribbon terranes, which can be continental or oceanic such as the Torricelli-Finisterre Arc accreted in the middle to late Miocene, or a composite continental-oceanic terrane such as the Sepik terrane accreted during the Eocene-Oligocene (Zahirovic et al., 2016b; Zahirovic et al., 2014). These accreted terranes are typically ~100 km across, and more than ~1000 km long. Northern New Guinea has also undergone periods of rifting and lithospheric rupture to form ocean basins including the Sepik back-arc ocean basin in the Late Mesozoic supported by syn-rift sedimentation in the Early-Mid Jurassic followed by a breakup unconformity (Davies, 2012; Zahirovic et al., 2016b; Zahirovic et al., 2014). The region has also experienced intra-oceanic subduction and proposed subduction polarity reversal episodes, including those associated with the consumption of the Sepik back-arc in the latest Cretaceous (Baldwin et al., 2012; Hill and Hall, 2003). This subduction history has resulted in a lack of preserved seafloor, compounded by poor outcrop due to weathering, vegetation cover and inaccessible terrain on the continent, which

76   results in significantly uncertain tectonic reconstructions (Hill and Hall, 2003; van

77   Ufford and Cloos, 2005; Zahirovic et al., 2014). Geologically, the northern half of the

78   island overlies Mesozoic crystalline basement of ocean crust with arc affinities

79   derived from the Pacific basin (Hill and Hall, 2003; van Ufford and Cloos, 2005),

80   whilst the southern portion comprises Mesozoic and Tertiary passive margin strata

81   underlain by Australian continental crust (Dow, 1977). The mountainous spine of the

82   island comprising the highly deformed Mobile Belt delineates the north and south of

83   New Guinea (Fig. 1).

84   In addition to the changing tectonic framework of New Guinea, the island also

85   experienced alternating periods of short-term (related to Milankovitch cycles) and

86   long-term (related to eustasy and mantle processes) inundation and emergence that

87   remain preserved in the sedimentary record (Fig. 2). Throughout Mesozoic times, the

88   continent was almost entirely inundated by shallow to deep seas with shelf-type and

89   deep-marine sediments dispersed across the island (Dow, 1977). In contrast, the late-

90   Eocene to early-Oligocene record is characterised by almost a total cessation in

91   sedimentation, with a distinct lack of lower to middle Oligocene fossils throughout

92   the oceanic crust and island arc terranes, particularly ordinarily pervasive foraminifera

93   (Dow, 1977). This is likely attributable to the combined effects of global sea level fall

94   (Haq, 2014; Haq et al., 1987) as well as the uplift and erosion corresponding to the

95   late Eocene-early Oligocene orogeny (Dow, 1977; van Ufford and Cloos, 2005). The

96   manifestation of this in the geological record is a pervasive, regional unconformity

97   (Fig. 2) (Norvick, 2001) except for a belt of mixed-grade metamorphics, in south-

98   eastern Papua New Guinea including the Owen Stanley and Emo metamorphics

99   which have been dated to between the Late Cretaceous and early Eocene (Worthing

100   and Crawford, 1996). This tectonic uplift is further supported by the late Eocene

101 intrusions in the north Sepik region along the marginal trough, and further south by

102 the vertical displacement of the Papuan Ultramafic Belt, along the Owen Stanley

103 Fault System (Davies, 2012; Dow, 1977). This non-depositional environment is

104 geologically short-lived with sedimentation resuming in the late Oligocene. Shallow-

105 water carbonates varying between 500 and 1500 m in thickness suggests flooding

106 peaked during the early- to mid-Miocene, despite inconsistencies with global sea level

107 estimates (Haq, 2014; Haq et al., 1987). From the Pliocene to the present, the flooding

108 somewhat retreated due to the combined effects of medium to short term sea level

109 change (Haq et al., 1987) as well as the shedding of debris from the accretion-related

110 mountains into the surrounding shallow shelf. The result today is a topographically

111 diverse and predominantly emergent island of New Guinea. Whilst the island likely

112 experienced short- and medium-term inundation patterns following regional sea-level

113 variations, the focus of this study is comparing long-term eustatic sea level (Haq,

114 2014; Haq et al., 1987) and long-term inundation and flooding indicated by

115 paleogeographic reconstructions.

116 Despite the well-documented paleogeographic record within New Guinea

117 (Dow, 1977; Norvick, 2003), there remain inconsistent correlations between the

118 mapped inundation patterns and global sea level curves (Haq, 2014; Haq et al., 1987).

119 Most previous work in the region has focused on unravelling the immense tectonic

120 complexity of New Guinea (Baldwin et al., 2012; Davies, 2012; Hill and Hall, 2003;

121 van Ufford and Cloos, 2005), with little focus on the role of deep Earth processes in

122 shaping the tectonic and topographic evolution of the northern Australian continental

123 margin. Such processes include subduction-driven mantle flow and its surface

124 expression of dynamic topography (Flament et al., 2013). Unlike crustal deformation

125 which occurs on spatial scales of 100 − 200 km resulting in elevations as large as

126 8 km, mantle-driven topography occurs over wavelengths of hundreds or thousands of

127 kilometres with amplitudes typically no greater than 1.5 km (Winterbourne et al.,

128 2014). Recent studies of Southeast Asia including that by Zahirovic et al. (2016a) and

129 Clements et al. (2011) have highlighted the importance of considering dynamic

130 topography to better understand the vertical motion of continents and their interaction

131 with eustatic sea level change. In Sundaland for example, Clements et al. (2011) and

132 Zahirovic et al. (2016a) linked regional dynamic uplift to plate tectonic history,

133 attributing its Late Cretaceous-Eocene emergence to the collision of Gondwana-

134 derived terranes and the associated subduction hiatus along the Sunda active margin.

135 Similar to Southeast Asia, over the last 160 Myr, the New Guinea margin has been

136 part of the complex convergence zone between Eurasian, Indo-Australian and Pacific

137 plates, which today manifests as a slab burial ground underlying much of the northern

138 half of Australia (Heine et al., 2010; Li et al., 2008; Ritsema et al., 2011; Sandiford,

139 2007). Consequently, New Guinea represents an important case study with which to

140 investigate the contribution of mantle flow to patterns of flooding and emergence.

141 This study extends upon the work by Husson et al. (2014) and to an extent that of

142 Flament et al. (2015) who explored the interplay of the plate-mantle system in

143 tectonically complex orogenic settings.

144 We use global plate reconstructions with regional refinements that are applied

145 as boundary conditions to forward geodynamic models to extract mantle evolution

146 and predicted dynamic topography. The dynamic topography trends are compared to

147 those interpreted from regional paleogeography and global sea level estimates. The

148 mantle flow models are qualitatively compared to the mantle structure inferred from

149 P- and S-wave seismic tomography.

150

151 **2. Methods**

152 **2.1 Estimating flooding from paleogeography**

153 Regional paleogeographic maps of Papua New Guinea from Dow (1977)

154 allowed us to identify shifting paleo-environments and constraints on flooding history

155 from the Jurassic to the present. Dow's (1977) compilation includes eight maps of

156 Papua New Guinea detailing patterns of sedimentation with a range of classifications

157 including land, marine shelf sediments (probable and outcropping), marine trough

158 (probable and outcropping), as well as basic delineations of outcropping volcanics

159 and metamorphics. These maps were digitised, georeferenced and where necessary

160 supplemented by the paleogeographic maps of Norvick (2003) to allow complete

161 coverage of the New Guinea continental margin (Fig. 3). Norvick (2003) and Dow's

162 (1977) facies maps were simplified to two discrete groupings of land and marine to

163 estimate flooding through time. To calculate the evolution of the extent of flooded

164 areas, the paleogeographic polygons were reprojected into a cylindrical equal area

165 coordinate system, with a central meridian of 145˚E and a standard parallel of 5˚S that

166 are appropriate for New Guinea. From this, total and percentage values of inundation

167 and emergence were calculated at the eight time intervals provided by Dow (1977),

168 and subsequently used for comparison to eustatic sea level curves and predicted

169 dynamic topography.

170

171 **2.2 Plate tectonic reconstructions**

172 Global plate motion models have evolved over many years of research with

173 the latest reconstructions representing a synthesis of previous tectonic models refined

174 and constrained through the accumulation of geological data. Due to the uncertainty

175 associated with poorly constrained regions, we tested two alternate plate

176 reconstructions for New Guinea presented in Zahirovic et al (2014) (Model A) and

177 Zahirovic et al (2016b) (Model B). These reconstructions are differentiated by

178 regional refinements that make it possible to test end-member tectonic scenarios (see

179 Table 1). Importantly, these scenarios are used as surface boundary conditions for

180 mantle flow models, providing the evolution of plate boundaries, plate velocities,

181 thermal lithospheric thicknesses for oceans and continents and slab buoyancy flux

182 (Bower et al., 2015). The vertical component of topography resulting from the

183 modelled mantle convection is extracted to generate dynamic topography predictions

184 (see Section 2.3).

185   In the New Guinea region, the major differences between the two plate

186 reconstructions primarily concern the timing of tectonic events. In the model of

187 Zahirovic et al. (2014) (Model A) the rifting on northern New Guinea, which resulted

188 in the separation of the Sepik terrane, occurs in Late Cretaceous times (Hill and Hall,

189 2003), whilst the latest model by Zahirovic et al. (2016b) (Model B) places this event

190 in latest Jurassic times (~172 Ma) (Table 1) (Davies, 2012). Consequently, the

191 opening of the Sepik ocean basin occurs significantly later in Model A compared to

192 Model B, which uses the supra subduction zone (SSZ) ophiolites in the Central Irian

193 Ophiolite Belt (likely of latest Jurassic age) to mark this opening at ~157 ± 16 Ma

194 (Table 1) (Permana, 1998). Regional volcanism in the Early Cretaceous and the

195 Kondaku Tuffs (Dow, 1977) support an active New Guinea margin by Early

196 Cretaceous times, as well as latest Jurassic SSZ ophiolites, which are likely a remnant

197 of the long-lived East Gondwana active margin (Zahirovic et al., 2016b).

198   It remains difficult to determine the longevity of this ocean basin as minimal

199 seafloor spreading history has been preserved. Model A uses a late Paleogene age of

200 ~35 – 31 Ma for the onset of north-dipping subduction along the Sepik as proposed by

201   Pigram and Davies (1987), whilst Model B uses the presence of ~68 Ma high-

202   temperature metabasites in the West Papuan Ophiolite as suggested by Davies (2012)

203   to support a significantly earlier age of subduction initiation at ~71 – 66 Ma (Table 1).

204   The New Guinea margin subsequently experienced two collisional phases; one in the

205   late Eocene to early Oligocene, the evidence for which remains preserved solely in

206   eastern New Guinea (Crowhurst et al., 1996), and a second, island-wide collisional

207   phase in Miocene times (Hill and Hall, 2003). In regards to the former, Zahirovic et al

208   (2014) (Model A) interpreted cooling histories derived from K-Ar thermochronology

209   in the New Guinea Mobile Belt to place the docking of the Sepik terrane between 27

210   – 18 Ma (Crowhurst et al., 1996). This is compared to Zahirovic et al.'s (2016b)

211   (Model B) slightly earlier interpretation of 35 – 31 Ma, that was based on the Ar-Ar

212   amphibolite age of Emo metamorphics, assuming the Sepik terrane docking was

213   contemporaneous with compression in the Papuan Peninsula (Table 1) (Worthing and

214   Crawford, 1996). It is likely that rather than representing alternate timing scenarios

215   for collision, these different age interpretations reflect the diachronous collision east-

216   west along the New Guinea margin.

217   Following this accretion, both reconstructions mark the presence of a south-

218   dipping subduction zone to the north of New Guinea that accounts for the ~18 – 8 Ma

219   Maramuni arc volcanism (Hill and Hall, 2003). The models differ in timing however,

220   with Model A placing the subduction between 15 – 5 Ma, compared to an earlier date

221   of ~20 – 10 Ma used in Model B (Table 1). The final phase of collision involved the

222   accretion of the Halmahera-Torricelli-Finisterre Arc. Model A uses apatite fission

223   track geochronology to mark the collision at ~6 Ma as proposed by Hill and Raza

224   (1999), whilst Model B uses an earlier collision age of ~14 Ma as evidenced through

225   K-Ar thermochronology (Table 1) (Crowhurst et al., 1996). As apparent, the complex

226 tectonic history of New Guinea has resulted in unresolved uncertainties in the plate

227 reconstructions, and thus testing multiple kinematic reconstructions allows us to

228 generate geodynamic scenarios that can be compared with the available surface

229 geology and mantle seismic tomography.

230

231 **2.3 Geodynamic modelling**

232　　We apply methods developed by Bower et al (2015) that incorporate plate

233 reconstructions into numerical models of mantle convection to predict past mantle

234 flow. Viscous incompressible mantle flow was computed using the Boussinesq

235 Approximation in the convection modelling code CitcomS (Zhong et al., 2008). To

236 calculate mantle flow, surface boundary conditions were imposed including global

237 plate velocities and lithospheric thicknesses derived from the plate reconstructions.

238 The surface boundary conditions such as the thermal structure of the lithosphere and

239 slabs above 350 km depth are progressively assimilated at 1 Myr time intervals

240 following Bower et al (2015). The implications of assimilating slab and lithosphere

241 structure is that the upper boundary layer is no longer dynamic (i.e., imposed), which

242 modifies the slab flux entering the mantle. However, due to the complex tectonic

243 history in this region and the deep-time nature of the evolution (i.e., since Jurassic

244 times), backward advection models (Conrad and Gurnis, 2003) are not suitable. In

245 addition, the focus of this study is on long-wavelength dynamic topography, which

246 primarily results from whole-mantle convection. All numerical models were

247 computed from 230 Ma to the present to capture post-Pangea break-up and allow the

248 flow models to reach a dynamic equilibrium from the initial conditions (Flament et

249 al., 2014). Initial conditions at 230 Ma include a slab insertion depth of 1400 km with

250 a dip angle of 45˚ above a depth of 425 km, and a dip angle of 90˚ below 425 km.

251   Further, to account for advective thickening (i.e., thickening due to an increase in

252   viscosity), the slabs are initially twice as thick in the lower mantle as in the upper

253   mantle in the initial condition at 230 Ma. The models are agnostic of mineral physics,

254   and include an initial basal thermochemical layer that is 113 km thick above the core-

255   mantle boundary, representing 2% of the volume of the mantle, consistent with the

256   seismically inferred value (Hernlund and Houser, 2008). The material in this layer is

257   3.6% denser than the ambient mantle, corresponding to a buoyancy ratio of 0.5. This

258   model set up supresses mantle plume formation thereby allowing for the subduction-

259   driven dynamic topography signal to be isolated (Flament et al., 2014). The

260   implications of this, as well as applying a non-adiabatic radial temperature profile and

261   disregarding internal heating, results in a lower mantle that is somewhat colder than

262   expected, with an overestimation of slab volumes.

263   The Rayleigh number (Ra) determines the vigour and style of convection, and

264   is defined by:

265
$$Ra = \frac{\alpha_0 \rho_0 g_0 \Delta T h_M^3}{\kappa_0 \eta_0}$$

266   where α is the coefficient of thermal expansivity, ρ the density, g the acceleration due

267   to gravity, ΔT the temperature difference between the surface and the CMB, h_M the

268   thickness of the mantle, κ the thermal diffusivity, η the dynamic viscosity, with the

269   subscript "0" indicating reference values (see Table 2). We varied the viscosity profile

270   based on stress and temperature, following

271
$$\eta = \eta_0(r) \exp \left(\frac{E_\eta}{R(T + T_\eta)} - \frac{E_\eta}{R(T_b + T_\eta)} \right)$$

272   where $\eta_0(r)$ is a depth-dependent and pre-defined value with respect to a reference

273   viscosity, E_η is the activation energy (E_{UM} in the upper mantle and E_{LM} in the lower

274   mantle), T is the temperature, T_η is a temperature offset, T_b is the ambient mantle

275   temperature, and *R* the universal gas constant. Whilst post-glacial rebound studies

276   reasonably constrain the viscosity of the upper mantle (Fjeldskaar et al., 2000;

277   Mitrovica and Forte, 2004), viscosity estimates of the lower mantle are less accurate

278   and thus our models are designed to test a range of possible scenarios (see Fig. 4).

279   Cases 1 to 3 are based on the plate reconstruction presented in Zahirovic et al (2014)

280   (Model A) with varying viscosity profiles, whilst a fourth case utilises the

281   reconstruction by Zahirovic et al. (2016b) (Model B). In each case, with respect to the

282   reference viscosity (η), the depth-dependent viscosity $\eta_0(r)$ is multiplied by a factor

283   of; 1 above 160 km; either 0.1 or 1 between 160–310 km depth (with and without an

284   asthenosphere respectively); 1 between 310–660 km depth; and either 100 or linearly

285   increasing from 10 to 100 in the lower mantle between 660 km and the core–mantle

286   boundary (CMB) (Fig. 4) (Steinberger and Calderwood, 2006). This radial viscosity

287   pre-factor is also applied to the assimilated slab material in the lower viscosity

288   asthenosphere. However, due to the temperature-dependent viscosity used in these

289   models, the slabs retain a larger relative viscosity than the asthenosphere. The

290   present-day volume-averaged viscosity for Case 4 is 41.6 x 10^{21} Pa s. Here, it is

291   important to test a range of viscosity scenarios for the lower mantle as it plays a

292   significant role in the observed dynamic topography trends, accounting for on average

293   58% of the observed signal as derived from Case 4 (Supp. Fig. 1). The average model

294   resolution, obtained with ~13 × 10^6 nodes and radial mesh refinement, is

295   ~50 × 50 × 15 km at the surface, ~28 × 28 × 27 km near the CMB, and ~40 × 40 ×

296   100 km in the mid-mantle. With this model setup, we hope to quantify some of the

297   uncertainty in the region by capturing possible end-member scenarios for the New

298   Guinea margin.

299   We computed time-dependent dynamic topography (h), at intervals of 10 Myr

300   from 230 Ma to the present following:

301
$$h = \frac{\sigma_{rr}}{\Delta\rho g_0},$$

302   where σ_{rr} and $\Delta\rho$ are the radial component of stress and the density difference

303   between the shallow mantle (ρ_{UM} = 3340 kg m^{-3}) and sea water (ρ_w = 1030 kg m^{-3})

304   respectively (see Table 2 for other parameters). Water-loaded dynamic topography is

305   calculated from the total normal stress resulting from mantle flow but excludes

306   buoyancy and lateral viscosity variations above a depth of 350 km, which is the

307   maximum depth to which slabs are inserted using time-dependent upper boundary

308   conditions (Bower et al., 2015). This results in a relatively low amplitude of dynamic

309   topography, as convection closer to the upper thermo-chemical boundary layer

310   generates stronger dynamic topography signals. However, due to the synthetic

311   insertion of slabs down to 350 km, the procedure to exclude these shallow depths is

312   necessary. The output dynamic topography and mantle evolution is then coupled with

313   the aforementioned plate reconstructions, to present a series of modelled snapshots

314   and vertical profiles from the latest Jurassic to the present (~160 – 0 Ma) (Fig. 5). In

315   addition, we extracted the predicted dynamic topography at specified points in New

316   Guinea (Figs 5 and 6) to obtain the point-specific evolution of dynamic topography

317   for all four cases from 160 Ma to the present (Fig. 7).

318

319   **3. Results**

320   **3.1 Comparison of predicted present-day mantle structure to seismic**

321   **tomography**

322   We qualitatively compare vertical profiles of predicted mantle temperature

323   (Fig. 5) to seismic tomography models (Fig. 8). Model temperature anomalies are

324 compared to seismic tomography velocity anomalies, assuming the latter result

325 primarily from thermal perturbations (Becker and Boschi, 2002; Grand, 2002). We

326 use a combination of P- and S-wave tomographic models, with the former providing

327 high resolution mantle imaging beneath subduction zones and continents

328 (Romanowicz, 2003), and the latter providing a more uniform global coverage of the

329 mantle and more equal sampling of the lower mantle (Grand, 2002). Whilst the

330 seismic tomography models share first-order similarities, they differ on scales smaller

331 then several hundreds of kilometres (Fig. 8) and this is due to model resolution, data

332 collection biases including the earthquake sources used and the earthquake relocations

333 applied as well as crustal correction and model parameterisation (Grand, 2002;

334 Romanowicz, 2008). Tomographic models have generally been shown to correlate

335 poorly with geodynamic models for spherical harmonic degrees $\geq$ 5 (Becker and

336 Boschi, 2002) and thus here we visually concentrate on long-wavelength correlations.

337 The high resolution P-wave models MIT-P08 (Li et al., 2008) (Fig. 8b) and GAP-P4

338 (Obayashi et al., 2013) (Fig. 8c) are utilised in conjunction with the S-wave models

339 S40rts (Ritsema et al., 2011) (Fig. 8d) and MontelliS (Montelli et al., 2006) (Fig. 8e).

340 Our numerical models exhibit reasonable compatibility with the positive

341 seismic velocity anomalies in P- and S-wave tomographic models (Fig. 8), with

342 Case 4 arguably generating the best match to mantle structure. In the mid-mantle,

343 notable discrepancies are observed between the four modelled cases, particularly

344 regarding the position of the Sepik slab which in Case 4 (Fig. 8) is located between

345 25˚S and 30˚S at a depth of approximately 1000 km. Though slightly underestimating

346 its volume, Case 4 reproduces good estimates for the depth and lateral position of the

347 subducted Sepik slab, compared to Cases 1–3 that display distinct lateral offsets.

348 These differences are likely attributable to the placement and timing of the associated

349   Sepik subduction zone, with the results supporting an earlier initiation of subduction

350   at ~70 Ma as modified in Model B by Zahirovic et al. (2016b). Similarly, Case 4

351   again produces better predictions of the Caroline slab in regard to both its depth and

352   geometry with correlations observed in both the P- and S-wave seismic tomography.

353   The Maramuni slab and northern New Guinea subduction do not fare as well, with all

354   cases seeing lateral offsets and incorrect estimations of slab volumes. These offsets

355   are likely a function of the model setup, particularly errors in the imposed subduction

356   history (Table 1), as well as the choice of radial viscosity (Fig. 4). Comparatively,

357   Model B (Zahirovic et al., 2016b) better predicts the depth of the Maramuni slab;

358   however, the interpretations regarding the northern New Guinea slab suggest further

359   plate reconstruction refinements are required. Overall, we note the better performance

360   of Case 4 in its reproduction of the mantle structure, with these observations

361   providing reasonable confidence in the associated dynamic topography predictions,

362   but also direction for future modifications to Model B, the plate tectonic

363   reconstruction by Zahirovic et al. (2016b) .

364

365   **3.2 Comparison of time-dependent dynamic topography to paleogeography**

366   The reasonable visual agreement between the mantle structure produced by

367   the flow models and seismic tomography models encourage us to analyse the time-

368   varying prediction of dynamic topography trends, which are likely to provide insight

369   into the dynamic uplift and subsidence of the region. The modelled evolution of

370   dynamic topography is characterised by periods of subsidence and uplift that are

371   similar to the alternating periods of flooding and emergence preserved in the regional

372   sedimentary record (Fig. 6). The dynamic topography signals varied only minimally

373   between the four tested scenarios, with the observed differences attributable primarily

374   to relative plate motions as well as variations in radial viscosity. In the models,

375   subduction history plays a key role in determining dynamic topography trends. The

376   paleogeographic record (Figs 2, 3 and 6a) provides a constraint with which to

377   compare our topography predictions. The mantle flow models present a period of

378   dynamic subsidence from the latest Jurassic to Early Cretaceous times (Fig. 6b) likely

379   associated with the descending slabs of the East Gondwana active margin. This

380   subsidence is consistent with the regional paleogeography, which records the

381   deposition of shallow and deep marine sediments (Fig. 2) and according to Dow

382   (1977) and Norvick (2003) represents a long period of continental inundation

383   (Fig. 6a). The gradual dynamic uplift that follows can be linked to slab roll-back of

384   the same East Gondwana subduction zone whereby dynamic subsidence associated

385   with the subducted slabs decreases, resulting in relative uplift of the surface (see

386   Digital Supplement). Regional dynamic subsidence was subsequently re-established

387   due to the onset of the north-dipping subduction of the Sepik oceanic basin. Here,

388   Cases 1–3 show a timing lag relative to Case 4, attributable to the later onset of the

389   Sepik subduction, initiating at ~ 35 Ma in the plate reconstruction of Zahirovic et al.

390   (2014) (Model A) compared to ~ 71 Ma in the plate reconstruction of Zahirovic et al

391   (2016b) (Model B). This timing offset is similarly observed in the final period of

392   dynamic subsidence throughout Miocene times, which in all cases is linked to the

393   south-dipping Maramuni Arc subduction zone on the northern margin of New Guinea.

394   In the latest plate motion model the Maramuni subduction is initiated at 23 Ma

395   compared to a later onset of 15 Ma in the earlier reconstruction, and this is manifest in

396   dynamic subsidence from 18 Ma in Case 4 compared to 8 Ma in Cases 1–3. This

397   period of dynamic subsidence is again validated using the paleogeographic record,

398   which preserves a history of widespread continental inundation throughout Miocene

399   times (Fig. 6).

400   We also compare modelled dynamic topography at specified points in New

401   Guinea, namely Irian Jaya (P1), central New Guinea (P2) and Papua New Guinea (P3)

402   (Fig. 1 and 5), to study the regional variation of subsidence and uplift trends (Fig. 7).

403   Moreover, with eastern and western New Guinea experiencing greater amplitudes of

404   dynamic change, these trends provide possible end-member scenarios on the signals

405   derived from central New Guinea, which is influenced by the Southeast Asian Sunda

406   slabs to the northwest and the New Guinea and Pacific slabs to the east (Figs 5 and 6).

407   Figure 7 highlights that whilst the general trends and timing are the same across all

408   point locations, eastern and western New Guinea experienced an opposite net

409   dynamic movement over time, with the downward continental tilt reversing from

410   eastward at 160 Ma, to westward at present. This long-term signal superimposed

411   beneath the temporally shorter dynamic topography trends highlights the complexity

412   and spatio-temporal variation of mantle dynamics influencing regional topography.

413   Furthermore, it must be emphasised that in a global context, New Guinea is a

414   relatively small continent located in a long-wavelength dynamic topography low (Fig.

415   5) and that the dynamic topography trends presented here primarily reflect the motion

416   of the continent over individual slabs associated with regional subduction systems.

417

418

419   **4. Discussion**

420   Our analysis suggests that inundation patterns through time in New Guinea

421   could be controlled by an interplay of deep Earth and surface processes. Our results

422   suggest a likely influence of dynamic topography on the long-term continental

423   flooding patterns of New Guinea since the Jurassic. Due to the difficulty in

424   constraining the amplitude of dynamic topography our analysis focuses on trends

425   rather than absolute values (Fig. 6). Of significance is the correlation between the two

426   periods of widespread flooding in New Guinea representing Cretaceous and Miocene

427   times (Figs 2, 3 and 6), and the modelled periods of dynamic subsidence. The

428   flooding of New Guinea from 145 – 90 Ma is influenced by high global sea levels

429   (Haq, 2014; Haq et al., 1987) amplified by dynamic subsidence linked to the East

430   Gondwana slab (Figs 5 and 6) (Zahirovic et al., 2016b). Gurnis et al. (1998) supported

431   the origin of this subducted slab based on the existence of a converging margin

432   between the Pacific plates and Gondwanaland since at least ~200 Ma. Similarly, they

433   explored the surface expression of this subducting slab focusing on the anomalous

434   vertical motion of eastern Australia throughout the Cretaceous (Gurnis et al., 1998).

435   Notably however, their modelled East Gondwana trench was a simplification of the

436   much more extensive Gondwanaland-Pacific margin, which they noted may have

437   extended further towards New Guinea. Here, we incorporate the northwestward

438   extension of this converging margin (Fig. 5), and link the contribution of this slab to

439   the continental subsidence of New Guinea.

440   During the Miocene, mantle dynamics hold greater significance with dynamic

441   subsidence trends alone correlating with the widespread inundation observed in New

442   Guinea (Fig. 6). During this time, all four scenarios present dynamic subsidence

443   corresponding to the subducted Maramuni slab, in contrast to global eustatic sea level

444   trends which are falling from ~35 Ma (Haq, 2014; Haq et al., 1987). Our models

445   suggest that sinking slabs are drawing the continent down faster than long-term sea

446   level is falling, causing regional flooding of New Guinea, similar to Southeast Asia

447   (Zahirovic et al., 2016). The models suggest this slab now resides in the lower mantle

448   at depths of between ~850 – 1350 km beneath the Gulf of Carpentaria (Fig. 8). This is

449   compatible with the work of Heine et al. (2010) and Sandiford (2007) who correlated

450   Australia's northward tilt since mid-Miocene times to a slab graveyard beneath

451   northern Australia.

452   In contrast, during the Paleogene, the predicted dynamic subsidence associated

453   with the subduction of the Sepik back-arc basin exhibits notably weaker correlations

454   with continental inundation as recorded by the paleogeography (Dow, 1977; Norvick,

455   2003). At times contemporaneous to the Sepik subduction and in the millions of years

456   following, New Guinea is characterised by regional uplift and a non-depositional

457   environment (Figs 3 and 6), as opposed to continental flooding. We suggest that

458   tectonic processes, including terrane collision and accretion associated with the

459   docking of the Sepik terrane in the late Eocene to early Oligocene, are likely

460   responsible for the observed margin-wide unconformity.

461   Indeed, the highly active tectonic setting of the region also demands the

462   consideration of tectonic processes in comprehensively isolating the mechanisms

463   behind regional flooding. For example, lithospheric flexure resulting from orogenic

464   loading is a plausible tectonic mechanism for continental subsidence (DeCelles and

465   Giles, 1996). Since Jurassic times, New Guinea has experienced two main periods of

466   orogenesis associated with the collision and accretion of Sepik terranes in early

467   Oligocene times (~35 – 31 Ma) and the accretion of the Halmahera-Torricelli-

468   Finisterre-Arc in mid-Miocene times (~14 Ma) (Zahirovic et al., 2016b). However, in

469   both cases the paleogeographic record provides clear evidence for the onset of

470   flooding prior to orogenesis, with marine sediments present from as early as the

471   ~66 Ma preceding the first collision, and ~25 Ma preceding the second collision (Fig.

472   2) (Dow, 1977; Norvick, 2003). This timeline suggests orogenic loading associated

473   with New Guinea's fold and thrust belts could not have initiated the observed

474   flooding. Work by Abers and Lyon‑Caen (1990) on the limited extent of eastern

475   New Guinea's foreland basin further supports this hypothesis. Their investigation

476   reveals that whilst the Australian plate underlying the foreland is relatively strong

477   with flexural rigidities of 10^{24} to 10^{25} Newton metres (Nm), localised plate weakening

478   beneath the eastern highlands results in a small and shallow foreland basin. Abers and

479   Lyon‑Caen (1990) suggested this weakness could be related to a combination of

480   thermal and mechanical processes resulting from Quaternary volcanism and thick-

481   skinned midcrustal faulting throughout the thrust belt. The overall result is that the

482   Australian lithosphere saw little deflection under the loading of New Guinea's eastern

483   highlands, with the foreland basin extending no more than 20 − 60 km from the

484   mountain front at present day (Abers and Lyon‑Caen, 1990). Others, including

485   Pigram et al. (1989), have investigated the development of the foreland basin since

486   the Oligocene and argue for a significantly larger flexural basin up to 600 -700 km

487   wide, south of the Fold and Thrust Belt. However, their analysis failed to incorporate

488   elastic thickness, which varied from 40 - 60 km in eastern Papua New Guinea to 70 -

489   80 km in the west (Haddad and Watts, 1999), which is incompatible with such

490   flexural basin widths. In the India-Eurasia collision zone for example, the elastic

491   thickness of the downgoing craton is estimated to be ~70-125 km, (ignoring the effect

492   of dynamic topography), with a foreland basin width of ~300 - 400 km (Jordan and

493   Watts, 2005; Tesauro et al., 2012). It is therefore unlikely that the large foreland basin

494   width on Papua New Guinea suggested by Pigram et al. (1989) is solely flexural, and

495   can rather be explained spatially and temporally with the addition of a dynamic

496   topography component from the south-dipping subduction related to the Maramuni

497   Arc, much like the manifestation of the Cretaceous-age epicontinental Western

498   Interior Seaway (USA) and the Eromanga Sea (Australia). The study by Husson et al.

499   (2014) provides a precedent for this argument with their results suggesting the uplift

500   history of the Himalayas and the subsidence of its foreland basin cannot be explained

501   without considering the effects of dynamic topography. In light of this, Husson et al

502   (2014) emphasises the need for revising estimates of elastic thickness to incorporate

503   the effects of dynamic topography in regions particularly effected by subduction-

504   driven mantle flow. In this regard, whilst lithospheric flexure likely played a minor

505   role in generating continental inundation, the regional flooding observed during the

506   Miocene (Figs 2, 3 and 6) cannot be explained without considering the effect of

507   mantle-driven dynamic topography during a time of global sea level fall. Through the

508   development of models that incorporate elastic thickness and foreland basin flexure,

509   the comparative contribution of these processes can be me more realistically

510   ascertained.

511   Despite the promising results presented here, these models, like all numerical

512   experiments, are inherently limited by their input parameters and simplifying

513   assumptions of complex Earth processes. For example, our current methods use rigid

514   plate motion models that do not incorporate continental deformation including the key

515   periods of orogenesis that characterise the tectonic history of our study area. Future

516   work should incorporate deforming plate reconstructions for the New Guinea margin

517   into forward geodynamic models. This would allow for the consideration of the

518   effects of crustal thickening associated with such collisions as that of the Sepik

519   terrane and the Halmahera-Finisterre-Torricelli Arc (Baldwin et al., 2012) on mantle

520   flow and dynamic topography. Moreover, future tectonic models should see

521   refinements to both the absolute plate motions in deep time and regional plate motions

522   towards present day that aim to correct for the lateral offsets and incorrect estimation

523   of slab volumes (Fig. 8).

524

525   **5. Conclusions**

526   Here we investigate the interplay of the plate-mantle system and its impact on

527   the vertical motion of continents in complex areas of orogeny. Using a case study of

528   the northern Australian continental margin we couple global plate reconstructions

529   with forward geodynamic models to predict the influence of the mantle flow on

530   ancient patterns of flooding and emergence. Our results provide support for

531   subduction driven dynamic uplift and subsidence from the Jurassic to the present,

532   with our model predictions being in agreement with the paleogeographic record. We

533   predict subduction at the East Gondwana margin prior to the Cretaceous provided a

534   positive feedback with higher eustatic sea levels to generate long-term regional

535   flooding. During the Miocene, however, subduction that produced the Maramuni arc

536   played a fundamental role in causing the widespread inundation, with evidence

537   suggesting contemporaneous long-term sea-level fall. As for the subduction of the

538   Jurassic-Cretaceous age Sepik back-arc basin, local collision and terrane accretion

539   masks its subsidence effect on New Guinea. Further research could explore the

540   potential surface expression of this slab in the tectonically quiescent region of

541   Australia.

542   To more confidently evaluate the role of tectonic processes in generating the

543   observed subsidence, further research may include the development of models that

544   consider orogenesis, elastic thickness and foreland flexure. Our analysis demonstrates

545   that deep Earth dynamics can be coupled to paleogeographic reconstructions of New

546 Guinea, providing new insights into the contribution of long-wavelength mantle flow

547 to the vertical motion of continents in areas of orogeny.

548

549

550

551

560

561 **Digital supplementary files**

562 We provide an animation for the evolution of predicted dynamic topography from

563 Case 4.

564

7. References

Abers, G.A., Lyon‑Caen, H., 1990. Regional gravity anomalies, depth of the foreland basin and isostatic compensation of the New Guinea Highlands. Tectonics 9, 1479-1493.

Baldwin, S.L., Fitzgerald, P.G., Webb, L.E., 2012. Tectonics of the New Guinea Region. Annual Review of Earth and Planetary Sciences 40, 495-520.

Becker, T.W., Boschi, L., 2002. A comparison of tomographic and geodynamic mantle models. Geochemistry, Geophysics, Geosystems 3.

Bower, D.J., Gurnis, M., Flament, N., 2015. Assimilating lithosphere and slab history in 4-D Earth models. Physics of the Earth and Planetary Interiors 238, 8-22.

Clements, B., Burgess, P.M., Hall, R., Cottam, M.A., 2011. Subsidence and uplift by slab-related mantle dynamics: a driving mechanism for the Late Cretaceous and Cenozoic evolution of continental SE Asia? Geological Society, London, Special Publications 355, 37-51.

Conrad, C.P., Gurnis, M., 2003. Seismic tomography, surface uplift, and the breakup of Gondwanaland: Integrating mantle convection backwards in time. Geochemistry, Geophysics, Geosystems 4.

Crowhurst, P., Hill, K., Foster, D., Bennett, A., 1996. Thermochronological and geochemical constraints on the tectonic evolution of northern Papua New Guinea. Geological Society, London, Special Publications 106, 525-537.

Davies, H.L., 2012. The geology of New Guinea-the cordilleran margin of the Australian continent. Episodes 35, 87-102.

DeCelles, P.G., Giles, K.A., 1996. Foreland basin systems. Basin research 8, 105-123.

Dow, D.B., 1977. A Geological Synthesis of Papua New Guinea, in: Resources, N. (Ed.). Australian Government Publishing Service, Canberra.

Fjeldskaar, W., Lindholm, C., Dehls, J.F., Fjeldskaar, I., 2000. Postglacial uplift, neotectonics and seismicity in Fennoscandia. Quaternary Science Reviews 19, 1413-1422.

Flament, N., Gurnis, M., Muller, R.D., 2013. A review of observations and models of dynamic topography. Lithosphere 5, 189-210.

Flament, N., Gurnis, M., Müller, R.D., Bower, D.J., Husson, L., 2015. Influence of subduction history on South American topography. Earth and Planetary Science Letters 430, 9-18.

Flament, N., Gurnis, M., Williams, S., Seton, M., Skogseid, J., Heine, C., Müller, R.D., 2014. Topographic asymmetry of the South Atlantic from global models of mantle flow and lithospheric stretching. Earth and Planetary Science Letters 387, 107-119.

Grand, S.P., 2002. Mantle shear–wave tomography and the fate of subducted slabs. Philosophical Transactions of the Royal Society of London A: Mathematical, Physical and Engineering Sciences 360, 2475-2491.

Gurnis, M., Müller, R.D., Moresi, L., 1998. Cretaceous vertical motion of Australia and the AustralianAntarctic discordance. Science 279, 1499-1504.

Haddad, D., Watts, A., 1999. Subsidence history, gravity anomalies, and flexure of the northeast Australian margin in Papua New Guinea. Tectonics 18, 827-842.

Haq, B.U., 2014. Cretaceous eustasy revisited. Global and Planetary Change 113, 44-58.

613   Haq, B.U., Hardenbol, J., Vail, P.R., 1987. Chronology of fluctuating sea levels since
614   the Triassic. Science 235, 1156-1167.
615   Heine, C., Müller, R.D., Steinberger, B., DiCaprio, L., 2010. Integrating deep Earth
616   dynamics in paleogeographic reconstructions of Australia. Tectonophysics 483,
617   135-150.
618   Hernlund, J.W., Houser, C., 2008. On the statistical distribution of seismic
619   velocities in Earth's deep mantle. Earth and Planetary Science Letters 265, 423-
620   437.
621   Hill, K.C., Hall, R., 2003. Mesozoic-Cenozoic evolution of Australia's New Guinea
622   margin in a west Pacific context. Geological Society of America Special Papers
623   372, 265-290.
624   Hill, K.C., Raza, A., 1999. Arc‐continent collision in Papua Guinea: Constraints
625   from fission track thermochronology. Tectonics 18, 950-966.
626   Husson, L., Bernet, M., Guillot, S., Huyghe, P., Mugnier, J.-L., Replumaz, A., Robert,
627   X., Van der Beek, P., 2014. Dynamic ups and downs of the Himalaya. Geology 42,
628   839-842.
629   Jordan, T., Watts, A., 2005. Gravity anomalies, flexure and the elastic thickness
630   structure of the India–Eurasia collisional system. Earth and Planetary Science
631   Letters 236, 732-750.
632   Li, C., van der Hilst, R.D., Engdahl, E.R., Burdick, S., 2008. A new global model for
633   P wave speed variations in Earth's mantle. Geochemistry, Geophysics,
634   Geosystems 9.
635   Matthews, K.J., Müller, R.D., Wessel, P., Whittaker, J.M., 2011. The tectonic fabric
636   of the ocean basins. Journal of Geophysical Research: Solid Earth 116.
637   Mitrovica, J., Forte, A., 2004. A new inference of mantle viscosity based upon joint
638   inversion of convection and glacial isostatic adjustment data. Earth and
639   Planetary Science Letters 225, 177-189.
640   Montelli, R., Nolet, G., Dahlen, F., Masters, G., 2006. A catalogue of deep mantle
641   plumes: New results from finite‐frequency tomography. Geochemistry,
642   Geophysics, Geosystems 7.
643   Norvick, M.S., 2001. Chronostratigraphic sections of the northern margins of the
644   Australian plate: final report. Unpublished report for AGSO.
645   Norvick, M.S., 2003. New paleographic maps of the northern margins of the
646   Australian plate: updated report. Unpublished report for Geoscience Australia.
647   Obayashi, M., Yoshimitsu, J., Nolet, G., Fukao, Y., Shiobara, H., Sugioka, H.,
648   Miyamachi, H., Gao, Y., 2013. Finite frequency whole mantle P wave tomography:
649   Improvement of subducted slab images. Geophysical Research Letters 40, 5652-
650   5657.
651   Permana, H., 1998. Dynamique de la mise en place des ophiolites d'Irian Jaya
652   (Indonésie), Thèse de doctorat de l'université de Nantes, p. 314.
653   Pigram, C., Davies, P., Feary, D., Symonds, P., 1989. Tectonic controls on
654   carbonate platform evolution in southern Papua New Guinea: Passive margin to
655   foreland basin. Geology 17, 199-202.
656   Pigram, C.t., Davies, H., 1987. Terranes and the accretion history of the New
657   Guinea orogen. BMR Journal of Australian Geology and Geophysics 10, 193-211.
658   Ritsema, J., Deuss, A., Van Heijst, H., Woodhouse, J., 2011. S40RTS: a degree-40
659   shear-velocity model for the mantle from new Rayleigh wave dispersion,
660   teleseismic traveltime and normal-mode splitting function measurements.
661   Geophysical Journal International 184, 1223-1236.

662 Romanowicz, B., 2003. Global mantle tomography: progress status in the past 10
663 years. Annual Review of Earth and Planetary Sciences 31, 303-328.
664 Romanowicz, B., 2008. Using seismic waves to image Earth's internal structure.
665 Nature 451, 266-268.
666 Sandiford, M., 2007. The tilting continent: a new constraint on the dynamic
667 topographic field from Australia. Earth and Planetary Science Letters 261, 152-
668 163.
669 Steinberger, B., Calderwood, A.R., 2006. Models of large-scale viscous flow in the
670 Earth's mantle with constraints from mineral physics and surface observations.
671 Geophysical Journal International 167, 1461-1481.
672 Tesauro, M., Audet, P., Kaban, M.K., Bürgmann, R., Cloetingh, S., 2012. The
673 effective elastic thickness of the continental lithosphere: Comparison between
674 rheological and inverse approaches. Geochemistry, Geophysics, Geosystems 13.
675 van Ufford, A.Q., Cloos, M., 2005. Cenozoic tectonics of New Guinea. AAPG
676 bulletin 89, 119-140.
677 Wessel, P., Smith, W.H., 1998. New, improved version of Generic Mapping Tools
678 released. Eos, Transactions American Geophysical Union 79, 579-579.
679 Wessel, P., Smith, W.H., Scharroo, R., Luis, J., Wobbe, F., 2013. Generic mapping
680 tools: Improved version released. Eos, Transactions American Geophysical Union
681 94, 409-410.
682 Winterbourne, J., White, N., Crosby, A., 2014. Accurate measurements of residual
683 topography from the oceanic realm. Tectonics 33, 982-1015.
684 Worthing, M., Crawford, A., 1996. The igneous geochemistry and tectonic setting
685 of metabasites from the Emo Metamorphics, Papua New Guinea; a record of the
686 evolution and destruction of a backarc basin. Mineralogy and Petrology 58, 79-
687 100.
688 Zahirovic, S., Flament, N., Dietmar Müller, R., Seton, M., Gurnis, M., 2016a. Large
689 fluctuations of shallow seas in low‐lying Southeast Asia driven by mantle flow.
690 Geochemistry, Geophysics, Geosystems 17, 3589-3607.
691 Zahirovic, S., Matthews, K.J., Flament, N., Müller, R.D., Hill, K.C., Seton, M., Gurnis,
692 M., 2016b. Tectonic evolution and deep mantle structure of the eastern Tethys
693 since the latest Jurassic. Earth-Science Reviews 162, 293-337.
694 Zahirovic, S., Seton, M., Müller, R., 2014. The Cretaceous and Cenozoic tectonic
695 evolution of Southeast Asia. Solid Earth 5, 227.
696 Zhong, S., McNamara, A., Tan, E., Moresi, L., Gurnis, M., 2008. A benchmark study
697 on mantle convection in a 3‐D spherical shell using CitcomS. Geochemistry,
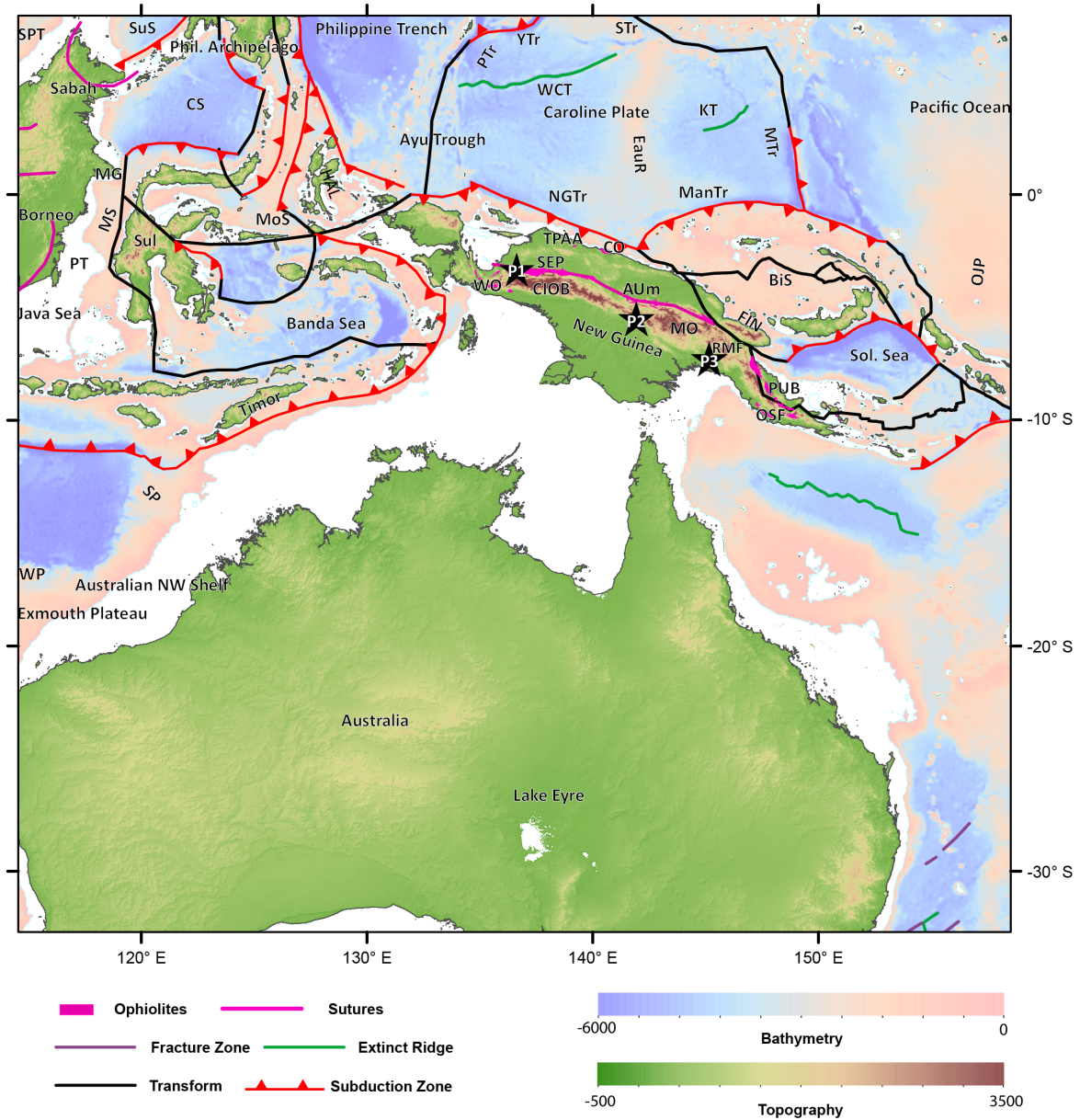698 Geophysics, Geosystems 9.
699
700

Figure 1. Regional tectonic setting of New Guinea and the northern Australian continental margin. Plate boundaries are modified from Bird (2003), ophiolites derived from Hill and Hall (2003) and Baldwin et al. (2012), and fracture zones from Matthews et al. (2011). Black stars with labels P1, P2 and P3 indicate locations from which dynamic topography values were extracted throughout time. Locations represent Irian Jaya, central New Guinea and Papua New Guinea respectively (see Fig. 7). AUm – April Ultramafics, BiS – Bismarck Sea, CIOB – Central (Irian) Ophiolite Belt, CO – Cyclops Ophiolite, CS – Celebes Sea, EauR – Eauripik Ridge, FIN – Finisterre Terrane, HAL – Halmahera, KB – Ketungau Basin, KT – Kiilsgaard Trough, ManTr – Manus Trench, MG – Mangkalihat, MTr – Mariana Trench, MO – Marum Ophiolites, MoS – Molucca Sea, MS – Makassar Straits, NGTr – New Guinea Trench, OJP – Ontong Java Plateau, OSF – Owen Stanley Fault, PT – Paternoster Platform, PUB – Papuan Ultramafic Belt, RMF – Ramu-Markham Fault, Sol. Sea – Solomon Sea, SP – Scott Plateau – SEP – Sepik, Sul – Sulawesi, TPAA – Torricelli-Prince Alexander Arc, WCT – W Caroline Trench, WO – Weyland Overthrust, WP – Wombat Plateau.
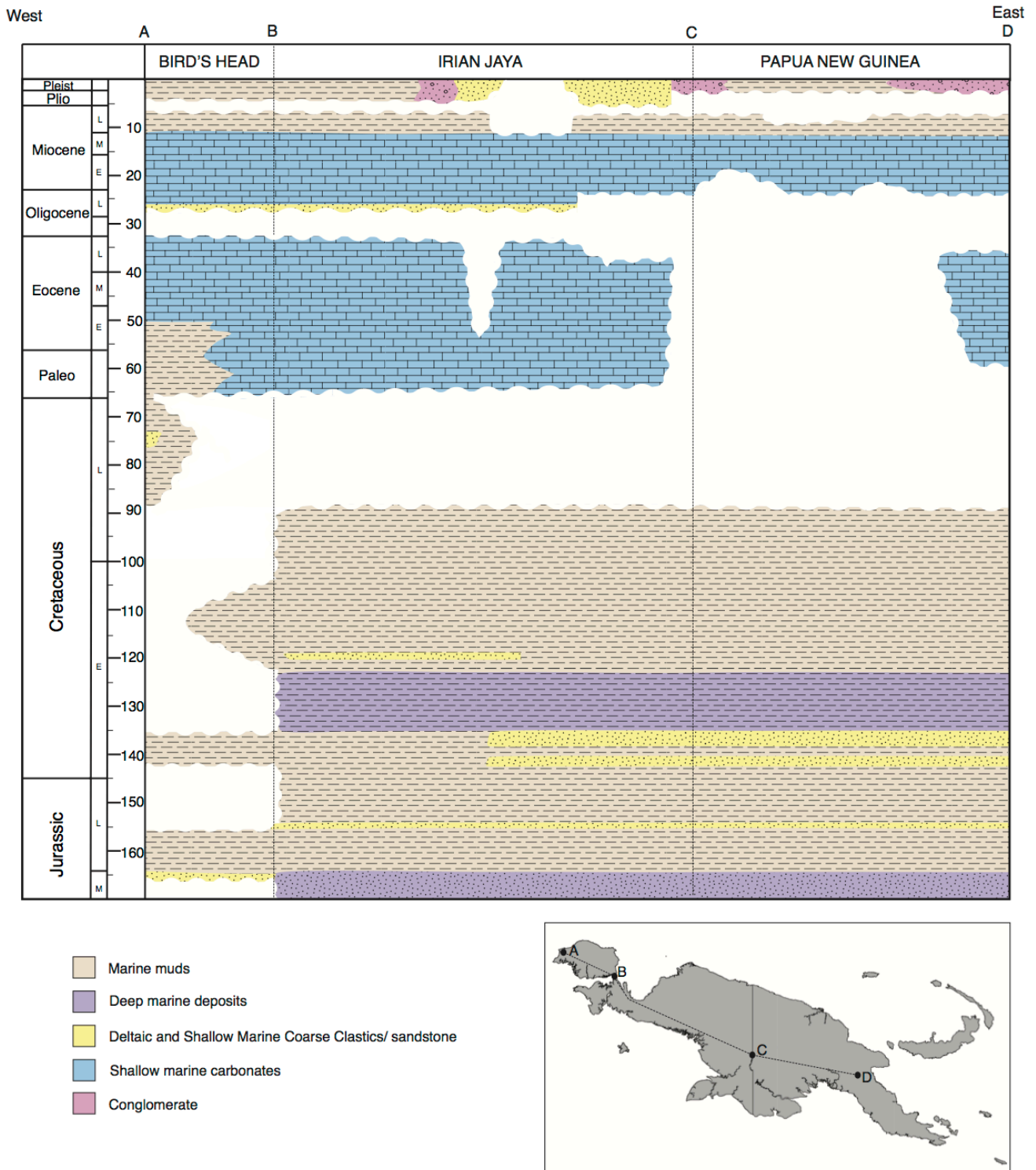
Figure 2. a) Simplified chronostratigraphic cross-section for New Guinea from the Middle Jurassic to the present, synthesised from Norvick (2001) and van Ufford and Cloos (2005). The stratigraphic sequence extends laterally from the north to the south of New Guinea (A-D) and is sub-divided based on the geographic boundaries Bird's Head, Irian Jaya and Papua New Guinea. This schematic highlights the Late Eocene to Oligocene regional unconformity, attributed to eustatic sea level fall and tectonic uplift resulting from the collision of the Australian and Pacific plates. Regional inundation throughout the Miocene is also apparent, with the geologic record preserving shallow marine carbonates, indicative of widespread shallow seas. b) Simplified map of New Guinea showing the A-D locations from which the stratigraphic sequence is delineated.
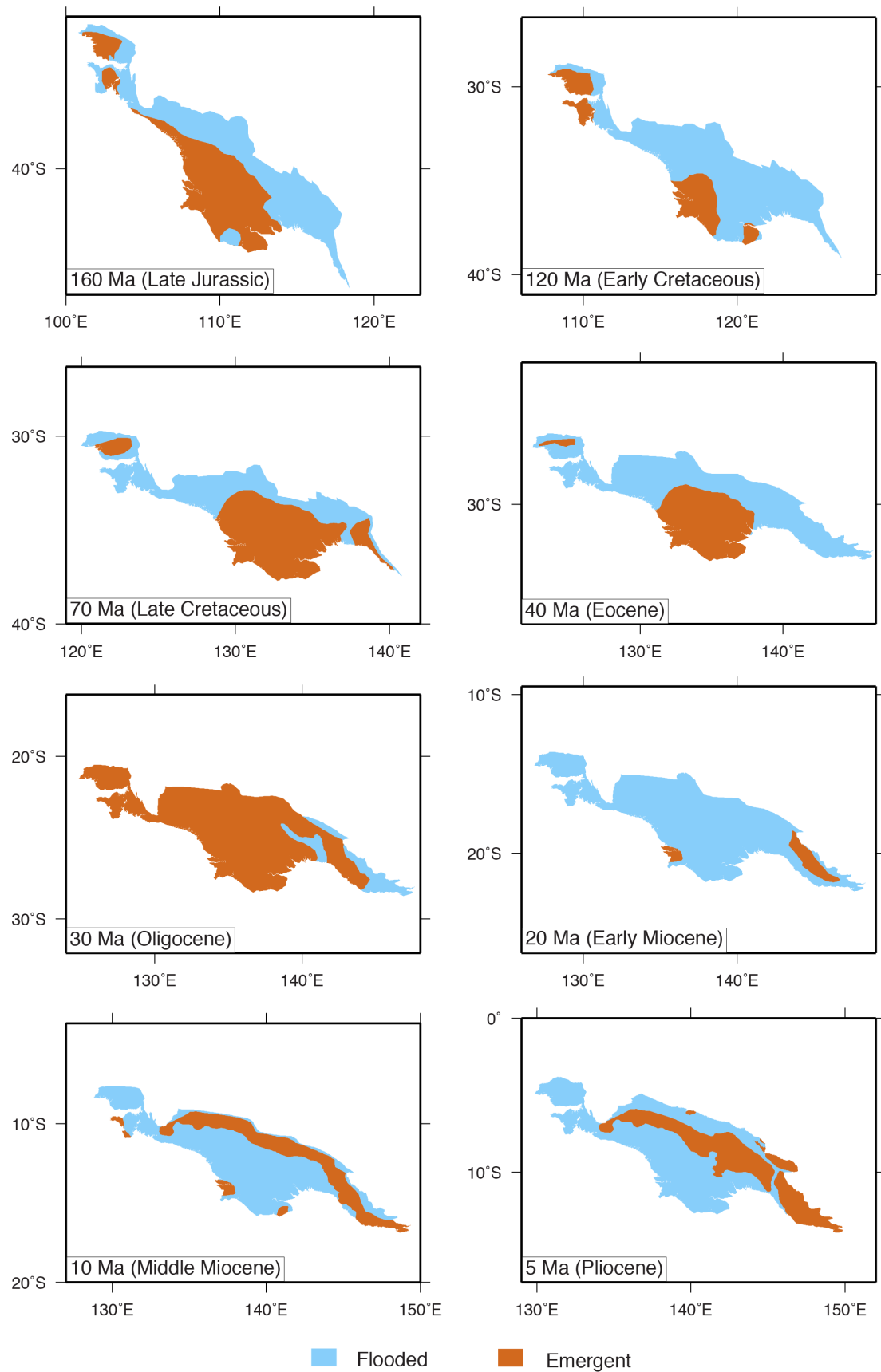
Figure 3. Paleo-environments of New Guinea from 160 – 0 Ma. The paleogeographies were digitised from Dow's (1977) and Norvick's (2003) patterns of sedimentation and attached to the plate reconstruction by Zahirovic et al (2016b). This paleogeographic reconstruction highlights the widespread inundation and sedimentary deposition throughout Miocene times, as well as the uplift and erosion environment that dominated during Oligocene times.
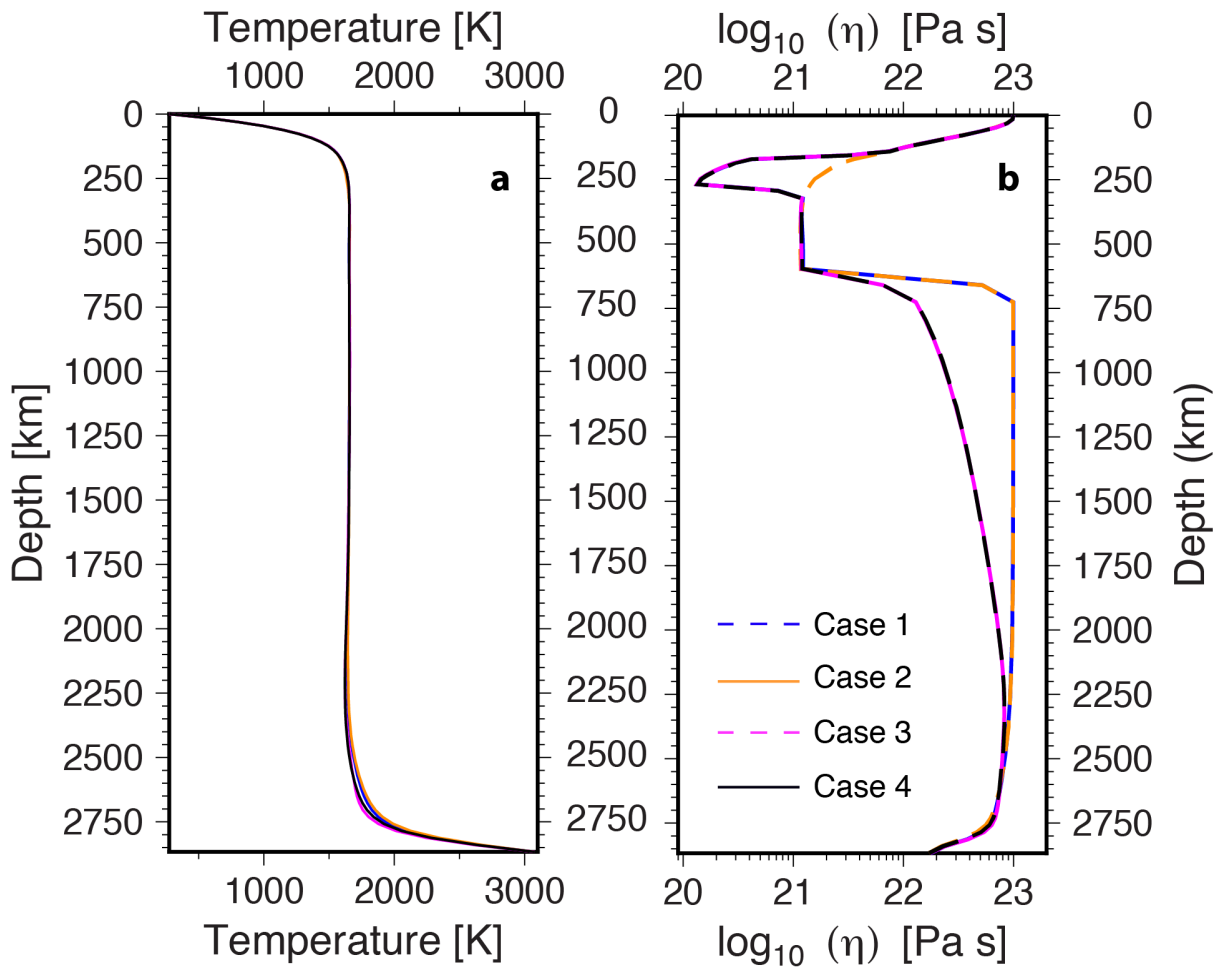
Figure 4: Horizontally averaged present-day a) mantle temperature and b) viscosity for Cases 1 – 4.
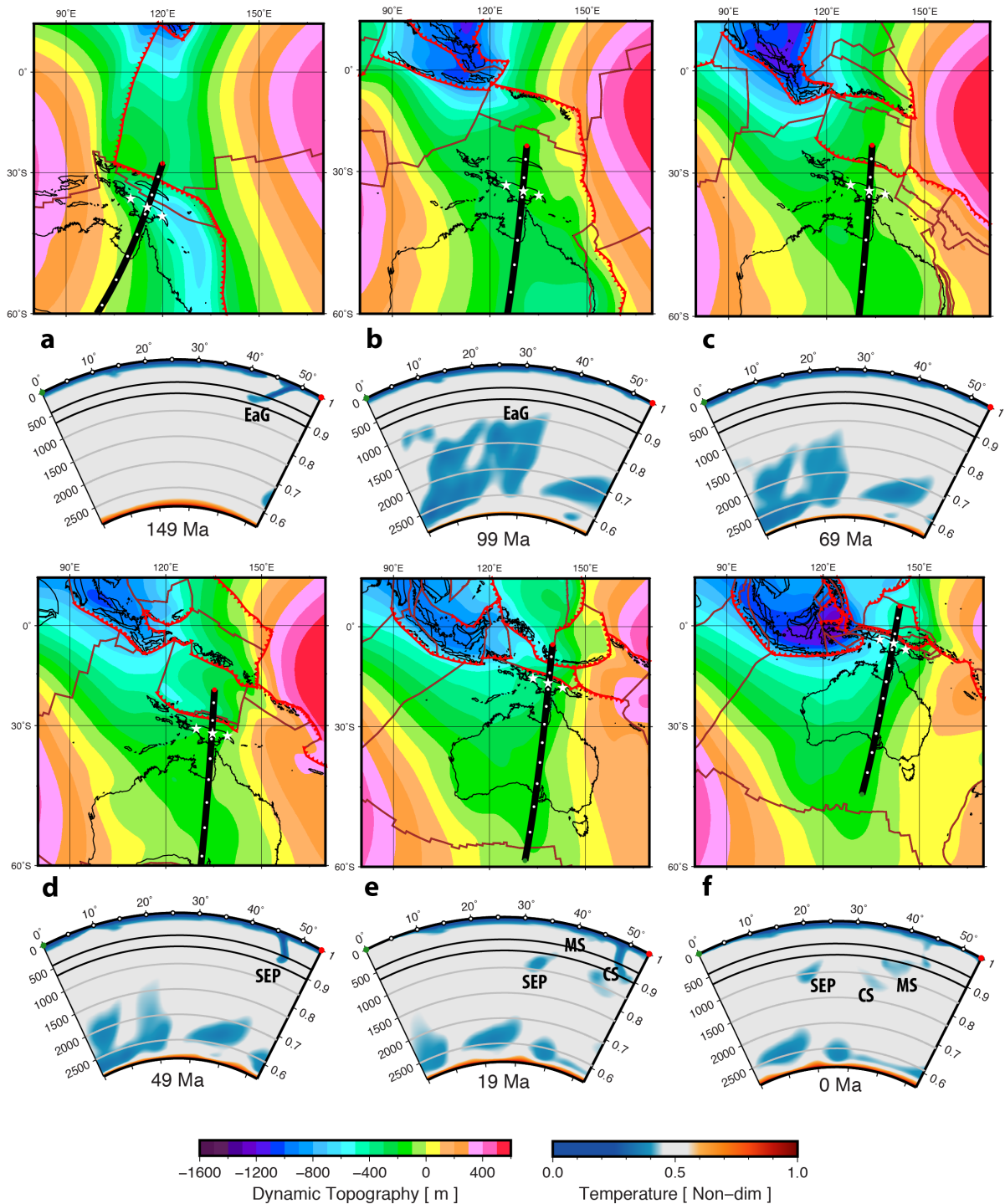
Figure 5. Dynamic topography and mantle temperature as predicted by Case 4. The evolution of modelled dynamic topography is presented within the tectonic framework of the region displaying subduction zones (red) and plate boundaries (brown). White stars indicate locations from which dynamic topography values were extracted throughout time (see Fig. 7). A great circle (thick black line, with white markers every 5 degrees) intersecting central New Guinea and eastern Australia has been reconstructed with the plate reconstruction of Zahirovic et al. (2016b). The evolution of mantle temperature is presented along this vertical profile from the surface to the core mantle boundary. In the Late Jurassic, tectonics in the northern Australian continental margin are dominated by the East Gondwana (EaG) active margin, with the first appearance of the EaG slab evident at ~150 Ma (a). This temperature anomaly dominates the mantle structure between New Guinea and Australia until the onset of north-dipping subduction of the Sepik (SEP) at ~70 Ma followed by south-dipping subduction of the Maramuni arc from ~23 – 15 Ma. MS – Maramuni Slab. CS – Caroline Slab.
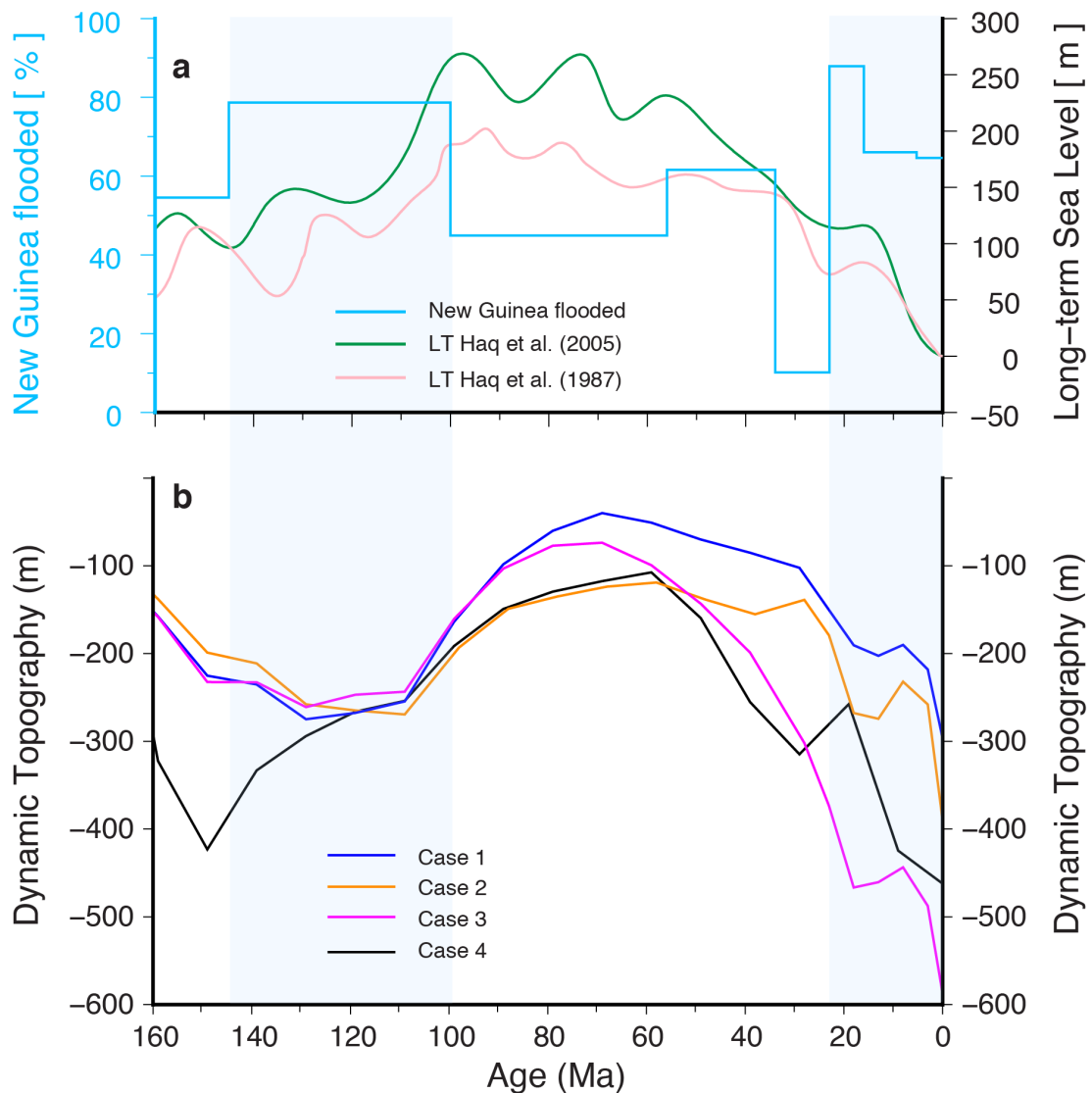
Figure 6. a) Continental inundation of New Guinea (blue) and long-term sea level derived from Haq et al (1987) and Haq et al (2005) (respectively lightpink and green). The comparative trends between sea level and flooding history highlight the discrepancies in correlating eustasy to inundation patterns. This is particularly evident during Early Miocene times when despite long-term falling sea levels, the continent is approximately 90% flooded. Such observations suggest the presence of another process influencing the continental inundation of New Guinea. b) Modelled dynamic topography signal of Cases 1–4 from central location in New Guinea (P2 in Fig.1). The trends of dynamic subsidence and uplift indicate a link to flooding and emergence patterns where eustasy explanations are lacking. The light blue shading that denotes regional flooding is generally correlated with dynamic subsidence (decreasing dynamic topography).
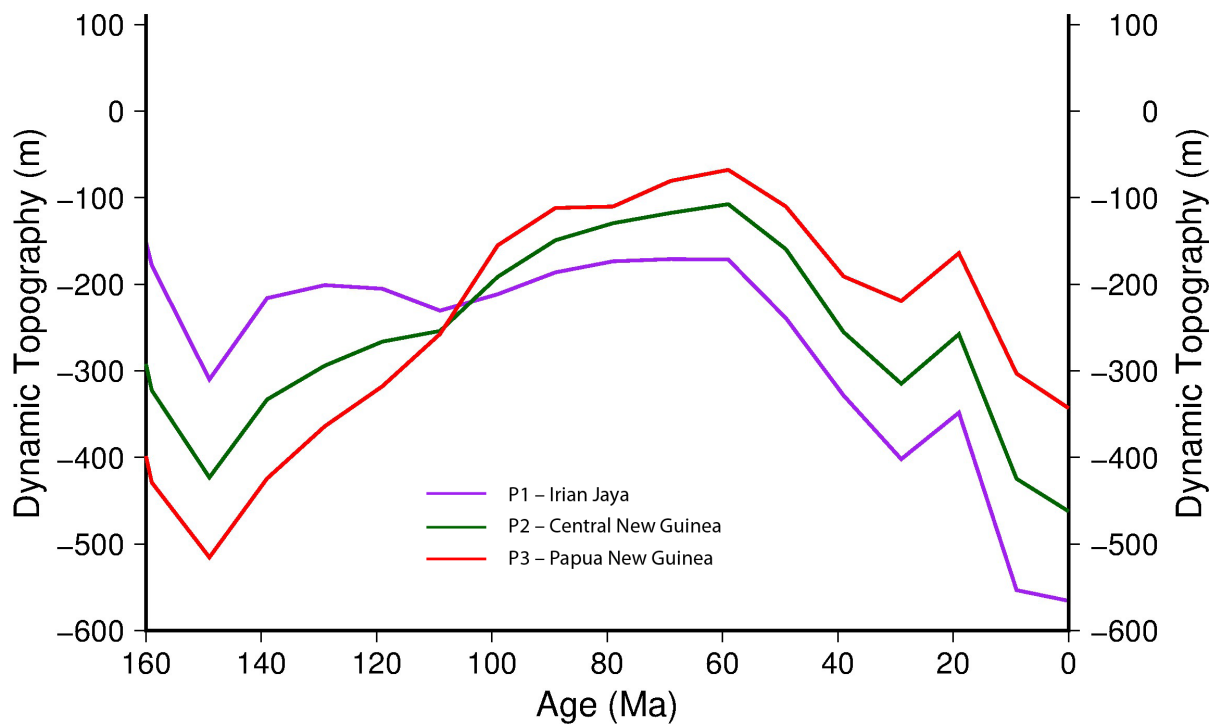
Figure 7. Modelled dynamic topography from three locations across New Guinea as depicted in Figures 1 and 5 for Case 4 (Zahirovic et al 2016b). The dynamic topography signals at Irian Jaya (west), central New Guinea and Papua New Guinea (east) display the same peaks and troughs over time, yet showcase an opposite net dynamic movement, with the downward continental tilt reversing from eastward at 160 Ma to westward at present.
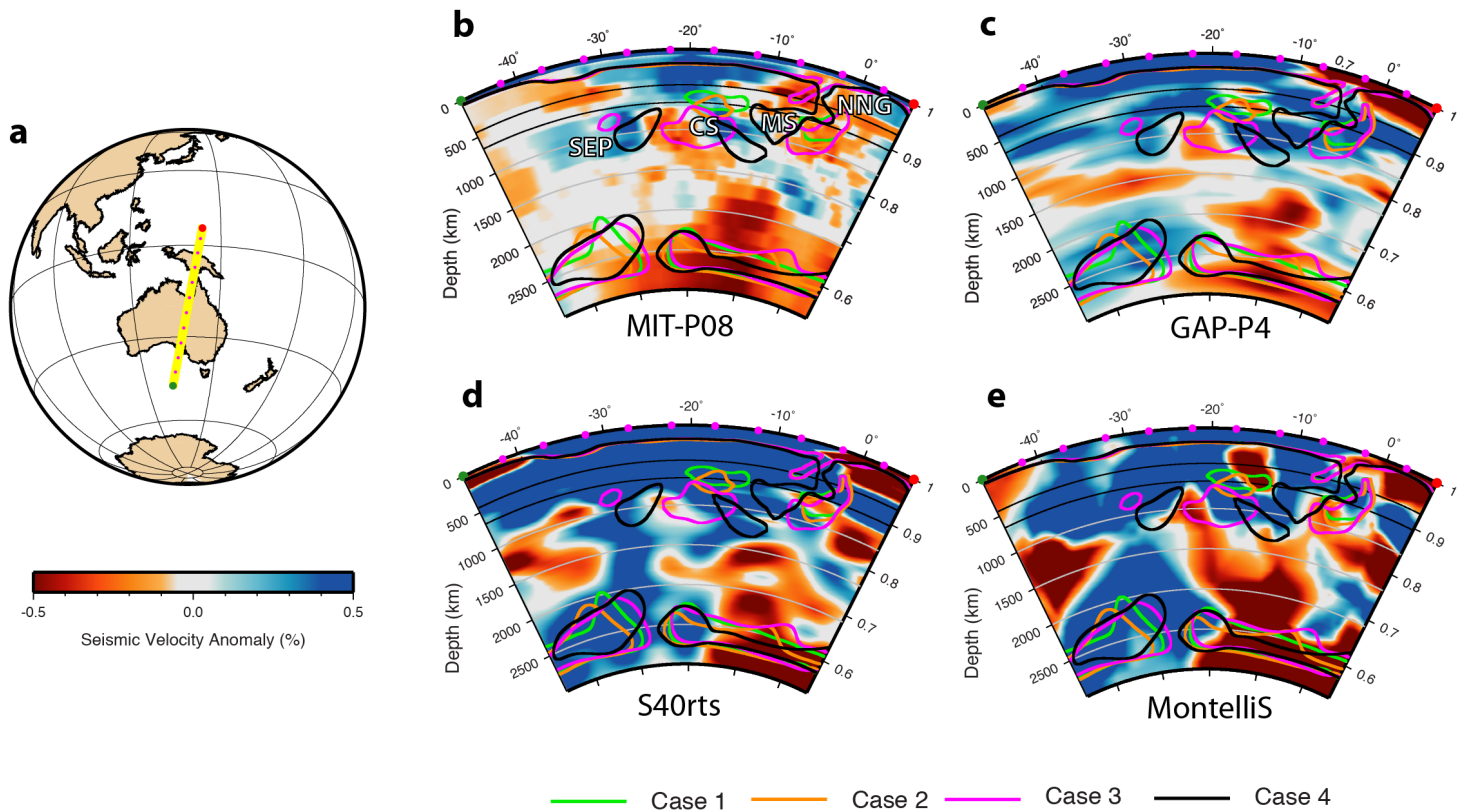
Figure 8. Comparison of geodynamic model predictions with seismic tomography models. The seismic tomography profiles are taken along the present-day transect depicted in a) encompassing central New Guinea and eastern Australia. We use P-wave tomographic models provided by Li et al. (2008) (b) and Obayashi et al. (2013) (c), and S-wave tomographic models provided by Ritsema et al. (2011) (d) and Montelli et al. (2006) (e). The overlying slab contours represent temperature anomalies from Cases 1–4, with the contours demarcating mantle 10% colder than ambient mantle temperature. Case 4 generates an overall better reproduction of the mantle structure, notably matching the Sepik slab (SEP) and the Caroline slab (CS) in both the P- and S- wave models. MS – Maramuni slab, NNG – Northern New Guinea slab.

711
712

**Table 1.** Comparison of Plate Tectonic Reconstructions

Feature	Zahirovic et al (2014) (Model A)	Zahirovic et al (2016) (Model B)
Rifting of the northern New Guinea margin	Late Cretaceous times	Late Jurassic times (~172 Ma)
Opening of the Sepik ocean basin	~80 Ma	~157 ± 16 Ma
Subduction polarity reversal and onset of north-dipping Sepik ocean basin subduction	~35 to 31 Ma	Maastrichtian times (~71 to 66 Ma)
Sepik terrane accretion to New Guinea	27 to 18 Ma	~35 to 31 Ma
South dipping subduction to the north of New Guinea	15 to 5 Ma	23 to 15 Ma
Halmahera-Torricelli-Finisterre Arc collision	~6 Ma	~14 Ma

713
714

Table 2. Parameters common to all model cases. Subscript "0" denotes reference values.

Parameter	Symbol	Value	Units
Rayleigh number	Ra	7.8×10^{7}	–
Thermal expansion coefficient	α_0	3×10^{-5}	K^{-1}
Density	ρ_0	4000	$kg\,m^{-3}$
Gravity acceleration	g_0	9.81	$m\,s^{-2}$
Temperature change	ΔT	2825	K
Temperature offset	T_η	452	K
Background mantle temperature	T_b	1685	K
Mantle thickness	h_M	2867	km
Earth radius	R_0	6371	km
Universal gas constant	R	8.31	$J\,mol^{-1}\,K^{-1}$
Thermal diffusivity	κ_0	1×10^{-6}	$m^2\,s^{-1}$
Reference Viscosity	η_0	1×10^{21}	Pa s
Activation energy (upper mantle)	$E_{\eta UM}$	100	$kJ\,mol^{-1}$
Activation energy (lower mantle)	$E_{\eta LM}$	33	$kJ\,mol^{-1}$
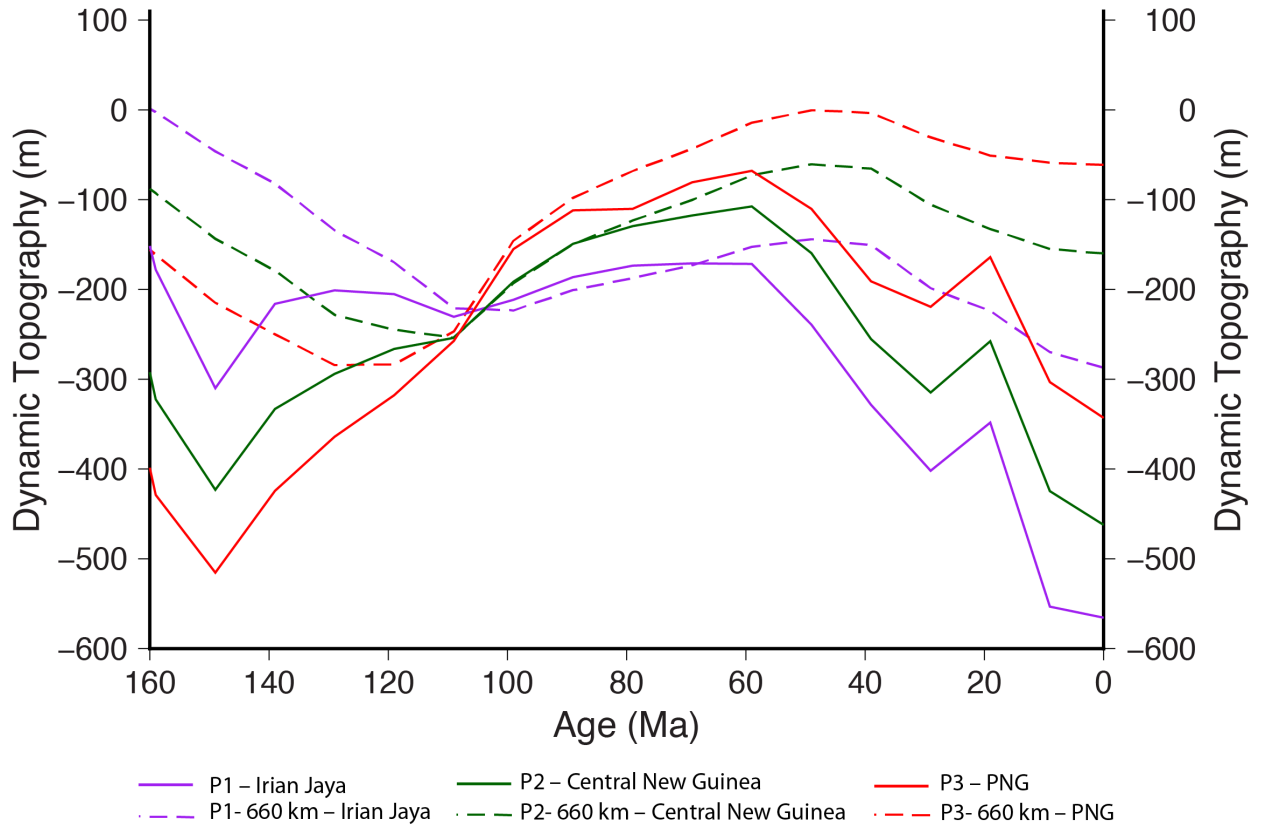
Supplementary Figure 1: Modelled dynamic topography from three locations across New Guinea for Case 4 (Zahirovic et al 2016b). The solid lines show the original dynamic topography signal as depicted in Fig. 7, whilst the dashed lines represent the dynamic topography signal from the lower mantle only, that is, from beneath the 660 km threshold. The figure shows that whilst the lower mantle controls much of the dynamic topography trends observed, it has a lower amplitude than that of the shallower signal.